Authors' Response to Reviews of

Assessing the Accuracy of a Three-Year High-Resolution Mesoscale Wind Farm Wake Simulation with Lidar and Satellite Radar Data

Alexandros Palatos-Plexidas on behalf of all authors
Wind Energy Science (WES) Journal,

RC: ***Reviewers' Comment***, AR: Authors' Response, □ Manuscript Text

1. Reviewer #3

RC: ***The paper presents a three-year WRF mesoscale simulation study of a Belgian–Dutch offshore wind-farm cluster, with and without the Fitch wind-farm parameterization. The simulations are validated using three offshore lidars, and model performance is evaluated for different stability conditions. The main question the paper addresses is the impact of the wind-farm parameterization on the results. The authors find that including the wind-farm parameterization in the mesoscale simulations improves accuracy in both intra-farm and downstream wakes.***

Overall, this is a well-designed study that uses quantitative metrics to assess performance across different boundary-layer stabilities. The addition of SAR data alongside the lidars is a clear strength. I have a few general comments and questions I would like the authors to address before I can recommend this work for publication.

AR: Dear Reviewer,
We sincerely thank you for your time and for the detailed and insightful comments. All changes and additions in the revised manuscript are highlighted in blue and enclosed in boxes.

We should also highlight that we have corrected the interpolation at hub-height for the BSB-lidar cases, resulting in a more accurate representation of the metrics throughout the full manuscript. More specifically, in the first version of the manuscript, we unintentionally used the lidar-measured heights without adding the BSB platform height of 45 m. This led to an incorrect estimation of both wind speed and wind direction at the intended hub height of 107 m.

1.1. General comments

RC: ***1. Is there a specific reason for focusing on only one height when the lidars provide velocities at multiple heights? Showing at least one representative vertical profile (e.g.,) would help illustrate the vertical structure of wakes and blockage.***

AR: Dear reviewer, thank you for your comment. We wanted to limit the already large scope and length of the paper, thus, we decided to limit the analysis to hub height, as this is most relevant for operational and planned wind turbines. However, we do agree that an analysis of profiles is interesting, and we would consider conducting it in future studies.

RC: ***2. Please comment on the criteria used to select the specific dates/times for the SAR analysis. Were they***

chosen based on visible wakes, wind direction, stability, or data availability? A short description of the selection process and potential selection bias would be helpful.

AR: SAR images cannot easily capture wind farm wakes, as they primarily provide wind speeds at approximately 10m height. In addition, only about 8–10 SAR snapshots per month cover the area of interest, and only a few of these contain sufficiently clear wake signatures. Furthermore, we were specifically interested in SW and NE wind directions affecting the Belgian–Dutch cluster, as these can generate wakes that propagate toward the WHi (located SW of the Belgian-Dutch cluster) and EPL (positioned NE the Belgian-Dutch cluster) lidar sites. As a result, the number of suitable SAR snapshots becomes even more limited. For this reason, we carefully selected the snapshots with clearly detectable long wake patterns (rather than short downstream deficits) to evaluate the WRF-WF performance during those cases. The snapshots are illustrative and may therefore reflect selection bias.

The overall text in Section 2.3.2, has been updated as follows (lines 191-201):

> The SAR data used in this study were retrieved by the Sentinel-1 European Space Agency mission. More specifically, there are two satellites, Sentinel-1A (2014-present) and Sentinel-1B (2016-2021), equipped with C-band Synthetic Aperture Radar (SAR) instruments operating at 5.405 GHz, and both satellites follow a sun-synchronous polar orbit at an altitude of 693 km [Hasager et al., 2024]. Focusing on the area of interest, including the Belgian-Dutch wind farms cluster in the Southern Bight of the North Sea, as well as additional upstream and downstream areas to study potential wake structures, the analyzed time instances occur approximately at 06:00 UTC every twelve days, and at 17:40 UTC every six days, respectively (Sentinel-1A, 2021-2023). The operation of Sentinel-1B during 2021 provided an additional set of overpasses at around 17:32 UTC every six days. This corresponds to approximately 8 to 10 SAR snapshots per month over the area of interest during the analyzed period. The wind speed at 10-meter height is then estimated by applying the CMOD5N geophysical model function [Hersbach et al., 2007], as explained also in the work of Siedersleben et al. [2020]. This indirect retrieval method assumes that radar backscatter from the sea surface, which reflects centimeter-scale waves generated by instantaneous wind stress, can be converted into wind speed at 10-meter height [Ahsbahs et al., 2017, 2018]. The wind fields are provided at a 500-meter pixel resolution through the Global Wind Atlas Science Portal of the Danish Technical University (DTU) Wind Energy Department (https://science.globalwindatlas.info/#/map/satwinds last access: 30 July 2025).

This has also been updated in Section 3.3., lines 504-510

> Four specific timestamps have been selected to analyze the wind speed patterns derived from SAR and WRF data, as well as to validate the model performance across the transect that connects the WHi, BSB, and EPL lidars (see Figure 2). These timestamps were selected manually based on the visual appearance of wind farm wakes in the SAR images. Although an average of 8 to 10 snapshots per month (see section 2.3.2) covers the analyzed region, the focus on wake events affecting the WHi, BSB, and EPL lidar sites under SW and NE wind directions resulted in a further reduction of the available snapshots. Therefore, an additional event from September 2020, outside the defined three-year simulation period, has been deliberately included for analysis.

RC: ***3. Is the surface roughness used in the SAR-based wind retrieval spatially variable in your analysis? How is this variability calculated or prescribed? A brief explanation of the roughness treatment should be added. In addition, how many SAR snapshots were analyzed in total, and what fraction of them showed clearly visible wakes?***

AR: Only 4 snapshots have been analyzed for this study, and they were manually selected based on visibly long wakes, as described in the previous comment 2.

Regarding the process of retrieving the wind fields from the satellite images, CMOD5N model has been used as explained in the updated Section 2.3.2 (lines 196-199, see comment 2 as well). However, we were not involved in this process, as the DTU database provides directly 10-meter retrieved wind speeds in netcdf format.

> The wind speed at 10-meter height is then estimated by applying the CMOD5N geophysical model function [Hersbach et al., 2007], as explained also in the work of Siedersleben et al. [2020]. This indirect retrieval method assumes that radar backscatter from the sea surface, which reflects centimeter-scale waves generated by instantaneous wind stress, can be converted into wind speed at 10-meter height [Ahsbahs et al., 2017, 2018].

RC: ***4. Is it possible to quantify the mean wake length for different stability classes (e.g., using a threshold deficit to define "wake end")? Even a simple diagnostic would strengthen the physical interpretation.***

AR: Since there are already a few studies discussing the wake characteristics (e.g., length) under different stability conditions Ali et al. [2023], Rosencrans et al. [2024], we considered updating our manuscript and assessing the mean wind speed deficit per stability class under the different wind speed regimes. More precisely, Figure 14 has been moved in Section 3.2.3, and it has been updated, including also the average wind speed deficit magnitude per wind speed magnitude class for each ABL stability regime (Figures 14C, and D). Below is the updated text in lines 453-477

> Figures 14A, and B present the frequency of the ABL stability conditions under the different wind speed ranges, for SW and NE wind directions, respectively. The ABL stability classification is based on Obukhov length, averaged across the three lidar probes in the NWF simulations. Under low wind speed conditions, very unstable and unstable events tend to dominate. Conversely, a transition toward near-neutral ABL stratification under high wind speeds is also evident. Previous studies [Rosencrans et al., 2024, Palatos-Plexidas et al., 2024, Porchetta et al., 2024] have demonstrated the dependence of wake propagation and wind speed losses on ABL stability, showing that transitioning from neutral to stable and very stable stratification, wakes tend to extend further downstream of wind farms. Similarly, we underscore the relation between wind speed magnitude, ABL stratification, and wake propagation, where during high wind speeds, the frequency of neutral events is enhanced and wakes propagate a few tens of kilometers downstream of the Belgian-Dutch cluster.
>
> In addition to the frequency of the stability regimes, in Figures 14C and D, the magnitude of the average normalized wind speed deficit is presented under the different stability conditions. The wind speed deficits are estimated as the average across the three analyzed lidar locations. It is observed that under very unstable and unstable occurrences, the wake magnitude is relatively lower (varying from 4 to 8%). When ABL stratification is near neutral, higher wake magnitudes are also observed. Following the patterns presented in studies [Rosencrans et al., 2024, Palatos-Plexidas et al., 2024, Porchetta et al., 2024], moving from unstable to neutral and stable stratification results in higher wind speed deficits. However, this should be interpreted together with the frequency of events in each wind speed class, which shows that the number of very stable cases, where wake effects are relatively strong, is not particularly large. On the other hand, the wind speed deficits during very unstable and unstable events that occur more frequently (especially when wind speeds are below 8 m s^{-1}) are significantly lower. Near neutral conditions occur more frequently when wind speed is above 8 m s^{-1} in both SW

and NE wind direction, and the wake magnitude in those cases ranges from about 7 to 12%. Greater wind speed magnitudes are associated with more pronounced downstream wind speed deficits (see Figures 12 and 13), as higher wind speeds in this region occur more frequently under neutral to stable conditions. Under these regimes, particularly during stable conditions, reduced turbulent mixing limits wake recovery, leading to enhanced and more persistent wakes [Rosencrans et al., 2024, Ali et al., 2023, Siedersleben et al., 2020]. The transition toward neutral and stable ABL conditions with the increasing wind speed may contribute to the higher cRMSE values observed in Tables 4 and 5, as these regimes are associated with enhanced shear.

In addition, we thought it might be useful to update our manuscript and discuss these characteristics, not under different ABL stratification, but under the different wind speed regimes as presented in Section 3.2.4. Therefore, we have updated Figure 15, including the 95% wake recovery areas (solid purple lines) and the maximum wake length within the area (dashed purple line). The characteristics of the wake are presented in Table 6. Section 3.2.4 has been updated in lines 479-501:

The analysis presented in the previous section, based on SW and NE wind directions, supports the investigation of the two-dimensional wake characteristics and blockage effects within the Belgian-Dutch wind farm cluster. A reduction in wind speed upstream of the wind farms is evident both under SW and NE wind directions. In the transect under SW winds (Figure 12), a noticeable wind speed deficit begins approximately 8 km upstream of the wind farm. This reduction is present across the different wind speed magnitudes, but becomes more rapid around 4 to 5 km upstream, particularly when wind speeds exceed 5 m s^{-1}. For NE wind directions (Figure 13), the blockage effect is also visible, though it is confined to a smaller region, approximately 2 to 3 km upstream of the Borssele wind farm.

The wake maps in Figure 15 further confirm the presence of blockage effects under both SW and NE wind conditions. The solid purple lines indicate the 95% wake recovery area, while the dashed purple lines represent the maximum wake length within this area for each wind speed regime and wind direction. The wake structures become less coherent at wind speeds below 5 m s^{-1} while an induction zone defined by the 95% wake recovery area is observed in low wind speeds. More precisely, the maximum blockage distance from the front row of the wind turbines appears around 10 km under SW wind direction (Figure 15A_1), whereas around 5 km in the NE wind direction regime (Figure 15A_2). In addition, Table 6 presents the values of the 95% wake recovery area and the maximum wake length within this area. The largest coherent wake region is extracted using connected-component labeling. Its perimeter is obtained from the contour of the binary mask, and the maximum extent is computed as the convex-hull diameter of the perimeter points. The estimation of both the 95% wake recovery area and the maximum wake length near SW or NE wind directions is performed using the SciPy Python package[Virtanen et al., 2020]. The values under the different wind speed regimes in Table 6 are comparable for both SW and NE wind directions.

When the flow transitions to higher wind speeds (above 5 m s^{-1}), the wake structures become more coherent, with more pronounced wake recovery areas, leading to overall longer wake lengths (see Table 6). In the 5–8 m s^{-1} class, a blockage region forms upstream of the turbines, extending approximately 8 to 9 km from the first row under both SW and NE conditions. At higher wind speeds, this blockage pattern becomes negligible, and the flow tends to deflect around the cluster and propagate farther downstream.

RC: ***5. Please discuss the limitations of using the Obukhov length diagnosed by the PBL scheme, particularly given that Monin–Obukhov similarity is known to break down in strongly stable conditions. How might this affect your stability classification and related conclusions?***

AR: There are limitations on the performance of Monin-Obukhov Similarity Theory (MOST), especially under strongly stable conditions. In addition, there are many studies that prefer using other stability metrics like Richardson number. However Obukhov length is still widely used (e.g., Rosencrans et al. [2024], Peña and Hahmann [2012], Quint et al. [2025], Archer et al. [2016]). Therefore, we considered that despite the uncertainties arising from MOST, and the configuration of surface and PBL schemes in WRF, the Obukhov length as a suitable metric to classify stability conditions.

In addition, a short comparison between the Obukhov length L and the bulk Richardson number Ri_b, both obtained from the NWF simulations as WRF outputs (RMOL and BR, respectively), is presented in Figure 1. The two metrics show consistent classification of the three principal stability regimes. The color scale indicates the percentage agreement, and only a small fraction of cases, 1.1% in stable conditions and 2.46% in unstable conditions, do not align. Nevertheless, it is important to note that while L allows a direct and widely used classification based on its sign (i.e., $L < 0$ for unstable, $L > 0$ for stable, and when $L \geq 500$ we consider neutral conditions), the choice of thresholds for Ri_b is less standardized. In this example, we apply $Ri_b < -0.001$ for unstable conditions, $Ri_b > 0.001$ for stable conditions, and consider the remaining near-zero values as neutral.

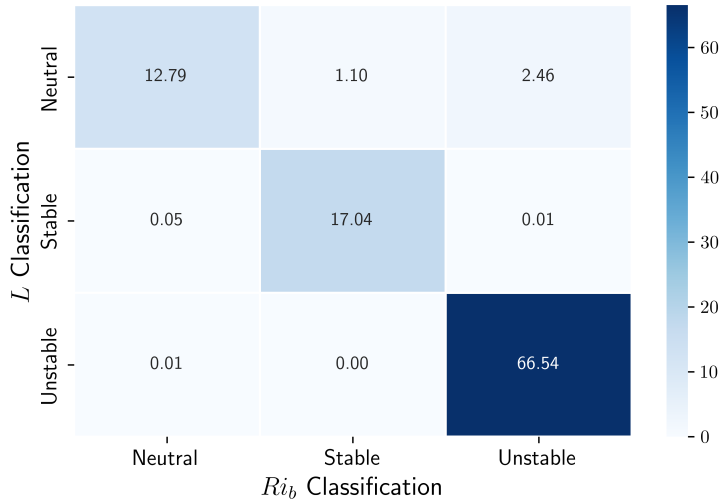

Figure 1: L and Ri_b on classifying stable, neutral, and unstable conditions.

We have updated the revised text in the results Section 3.2.2., as follows in lines 365-369:

> The increase in cRMSE under very stable conditions is also reflected in the Pearson correlation, which decreases when transitioning from stable-neutral to very stable regimes. At BSB, all wind speed metrics improve in the WF simulations relative to the NWF runs across the different stability regimes, even under very stable conditions that are known to be associated with enhanced wakes [Rosencrans et al., 2024, Ali et al., 2023, Siedersleben et al., 2020]. These findings align with the correlation analysis between WRF and sonic anemometer measurements in the Horns Rev wind farm [Peña and Hahmann, 2012], which shows that model uncertainty increases as atmospheric stability deviates from neutral, i.e., under very stable or very unstable conditions. Although the Obukhov length diagnosed by the PBL scheme becomes uncertain under strongly stable conditions when Monin–Obukhov similarity theory

is known to break down [Stiperski and Calaf, 2023, Optis et al., 2016] due to weak or intermittent turbulence, it remains a fundamental and practical metric for characterizing ABL stability in mesoscale models. Despite its limitations, many studies use Obukhov length, as it provides a consistent, physically based framework for classifying stability regimes and interpreting wake behaviour [Rosencrans et al., 2024, Quint et al., 2025].

We consider that the conclusion of the study remains robust, as the Obukhov length still provides the most practical and physically grounded metric for categorizing stability conditions in mesoscale simulations, and the key patterns we report are not sensitive to small shifts in stability class, as the number of very-stable events where the MO similarity theory can break is relatively small.

1.2. Specific comments

RC: ***1. Instead of referring only to the lidars by their site names, it may improve readability to also refer to them by their functional roles (e.g., "upwind/free-stream," "intra-farm," and "far-wake" or "downstream") throughout the text.***

AR: We have improved the manuscript in Sections 3.2.3, 3.2.4, and 3.3, where we discuss the wind farm transects to highlight the positions of the lidars as upstream, intra-farm, and downstream. For example, in the updated Figure 15, there is a distinction of free-stream and down-stream locations. Similarly, in Table 7, which presents the metrics on the SAR events analysis.

RC: ***2. Providing the WRF namelist file (at least for the innermost domain) as supplementary material would significantly help reproducibility.***

AR: We will be happy to share our WRF-configuration files upon request. The code availability statement on the manuscript has been updated accordingly.

RC: ***3. Figure 7 uses "r" for the correlation coefficient, whereas Figures 6 and 8 use "ρ" Please standardize the notation across figures for consistency.***

AR: We use the distinction between r and ρ. r is the Pearson correlation coefficient, and it is defined for wind speed (and linear variables in general), while ρ is the circular (directional) correlation coefficient. Although both estimate the correlation between the observations and the simulations, their definitions differ. The equations are provided in the Appendix, and lines 238-239 have been added in Section 2.3.4.

To compute means on the wind direction, the circular means are applied [Mardia and Jupp, 2009]. The cRMSE equation for circular variables (A6) has been adopted from the study of [Rosencrans et al., 2024]. Instead of the Pearson correlation for linear values, the circular-circular correlation ρ is used [Mardia and Jupp, 2009]. All metrics are computed using the built-in functions of the NumPy [Harris et al., 2020] and SciPy [Virtanen et al., 2020] Python packages. Furthermore, the *wasserstein_circle* function by the Python Optimal Transport [Flamary et al., 2021] package is used to calculate the EMD for the wind direction.

References

T. Ahsbahs, M. Badger, P. Volker, K. S. Hansen, and C. B. Hasager. Applications of satellite winds for the offshore wind farm site anholt. *Wind Energy Science*, 3(2):573–588, 2018. . URL `https:`

//wes.copernicus.org/articles/3/573/2018/.

Tobias Ahsbahs, Merete Badger, Ioanna Karagali, and Xiaoli Guo Larsén. Validation of sentinel-1a sar coastal wind speeds against scanning lidar. *Remote Sensing*, 9(6), 2017. ISSN 2072-4292. . URL https://www.mdpi.com/2072-4292/9/6/552.

Karim Ali, David M Schultz, Alistair Revell, Timothy Stallard, and Pablo Ouro. Assessment of five wind-farm parameterizations in the weather research and forecasting model: a case study of wind farms in the north sea. *Monthly Weather Review*, 151(9):2333–2359, 2023. URL https://doi.org/10.1175/MWR-D-23-0006.1.

Cristina L Archer, Brian A Colle, Dana L Veron, Fabrice Veron, and Matthew J Sienkiewicz. On the predominance of unstable atmospheric conditions in the marine boundary layer offshore of the us northeastern coast. *Journal of Geophysical Research: Atmospheres*, 121(15):8869–8885, 2016. URL https://doi.org/10.1002/2016JD024896.

Rémi Flamary, Nicolas Courty, Alexandre Gramfort, Mokhtar Z Alaya, Aurélie Boisbunon, Stanislas Chambon, Laetitia Chapel, Adrien Corenflos, Kilian Fatras, Nemo Fournier, et al. Pot: Python optimal transport. *Journal of Machine Learning Research*, 22(78):1–8, 2021. URL http://jmlr.org/papers/v22/20-451.html.

Charles R. Harris, K. Jarrod Millman, Stéfan J. van der Walt, Ralf Gommers, Pauli Virtanen, David Cournapeau, Eric Wieser, Julian Taylor, Sebastian Berg, Nathaniel J. Smith, Robert Kern, Matti Picus, Stephan Hoyer, Marten H. van Kerkwijk, Matthew Brett, Allan Haldane, Jaime Fernández del Río, Mark Wiebe, Pearu Peterson, Pierre Gérard-Marchant, Kevin Sheppard, Tyler Reddy, Warren Weckesser, Hameer Abbasi, Christoph Gohlke, and Travis E. Oliphant. Array programming with NumPy. *Nature*, 585(7825):357–362, September 2020. . URL https://doi.org/10.1038/s41586-020-2649-2.

Charlotte Bay Hasager, James Imber, Jana Fischereit, Aito Fujita, Krystallia Dimitriadou, and Merete Badger. Wind speed-up in wind farm wakes quantified from satellite sar and mesoscale modeling. *Wind Energy*, 27 (11):1369–1387, 2024. URL https://doi.org/10.1002/we.2943.

H. Hersbach, A. Stoffelen, and S. de Haan. An improved c-band scatterometer ocean geophysical model function: Cmod5. *Journal of Geophysical Research: Oceans*, 112(C3), 2007. . URL https://agupubs.onlinelibrary.wiley.com/doi/abs/10.1029/2006JC003743.

Kanti V Mardia and Peter E Jupp. *Directional statistics*. John Wiley & Sons, 2009. .

Michael Optis, Adam Monahan, and Fred C. Bosveld. Limitations and breakdown of monin–obukhov similarity theory for wind profile extrapolation under stable stratification. *Wind Energy*, 19(6):1053–1072, 2016. . URL https://onlinelibrary.wiley.com/doi/abs/10.1002/we.1883.

Alexandros Palatos-Plexidas, Simone Gremmo, Sara Porchetta, Jeroen Van Beeck, Lesley De Cruz, and Wim Munters. A numerical analysis of wind farm wake characteristics in the southern part of the north sea. *Journal of Physics: Conference Series*, 2767(9):092078, jun 2024. . URL https://dx.doi.org/10.1088/1742-6596/2767/9/092078.

Alfredo Peña and Andrea N. Hahmann. Atmospheric stability and turbulence fluxes at horns rev—an intercomparison of sonic, bulk and wrf model data. *Wind Energy*, 15(5):717–731, 2012. . URL https://onlinelibrary.wiley.com/doi/abs/10.1002/we.500.

S. Porchetta, M. F. Howland, R. Borgers, S. Buckingham, and W. Munters. Annual wake impacts in and between wind farm clusters modelled by a mesoscale numerical weather prediction model and fast-running engineering models. *Wind Energy Science Discussions*, 2024:1–37, 2024. . URL https://wes.copernicus.org/preprints/wes-2024-58/.

D. Quint, J. K. Lundquist, and D. Rosencrans. Simulations suggest offshore wind farms modify low-level jets. *Wind Energy Science*, 10(1):117–142, 2025. . URL https://wes.copernicus.org/articles/10/117/2025/.

D. Rosencrans, J. K. Lundquist, M. Optis, A. Rybchuk, N. Bodini, and M. Rossol. Seasonal variability of wake impacts on us mid-atlantic offshore wind plant power production. *Wind Energy Science*, 9(3): 555–583, 2024. . URL https://wes.copernicus.org/articles/9/555/2024/.

S. K. Siedersleben, A. Platis, J. K. Lundquist, B. Djath, A. Lampert, K. Bärfuss, B. Cañadillas, J. Schulz-Stellenfleth, J. Bange, T. Neumann, and S. Emeis. Turbulent kinetic energy over large offshore wind farms observed and simulated by the mesoscale model wrf (3.8.1). *Geoscientific Model Development*, 13(1): 249–268, 2020. . URL https://gmd.copernicus.org/articles/13/249/2020/.

Ivana Stiperski and Marc Calaf. Generalizing monin-obukhov similarity theory (1954) for complex atmospheric turbulence. *Phys. Rev. Lett.*, 130:124001, Mar 2023. . URL https://link.aps.org/doi/10.1103/PhysRevLett.130.124001.

Pauli Virtanen, Ralf Gommers, Travis E Oliphant, Matt Haberland, Tyler Reddy, David Cournapeau, Evgeni Burovski, Pearu Peterson, Warren Weckesser, Jonathan Bright, et al. Scipy 1.0: fundamental algorithms for scientific computing in python. *Nature methods*, 17(3):261–272, 2020. URL https://doi.org/10.1038/s41592-019-0686-2.